Contents lists available at ScienceDirect

Transactions of Nonferrous Metals Society of China

36(2026) 401−415

www.tnmsc.cn

Microstructural evolution and mechanical properties of electron beam welded 5B70 aluminum alloy joint

Yu-peng ZHANG [a], Guo JIN [a,*], Li-hong DONG [b,**], Xiu-fang CUI [a], Chong GAO [c], Xiang-yu XIE [a], Yue-lan DI [b], Wei-ling GUO [b], Ya-ya SONG [b], Wen-jing SHI [d], Ru-chuan ZENG [e], Ning HUANG [e]

[a] Key Laboratory of Superlight Material and Surface Technology of Ministry of Education, College of Materials Science and Chemical Engineering, Harbin Engineering University, Harbin 150001, China;

[b] National Key Laboratory for Remanufacturing, Army Academy of Armored Forces, Beijing 100072, China;

[c] College of Mechanical Engineering and Automation, Liaoning University of Technology, Jinzhou 121001, China;

[d] Beijing Institute of Spacecraft System Engineering, Beijing 100094, China;

[e] Beijing Spacecraft Manufacturing Co., Ltd., Beijing 100089, China

Abstract: The microstructural evolution and mechanical properties of a vacuum electron beam welded aerospace 5B70 aluminum alloy joint were studied. Quantitative analyses of the phase composition, microstructural evolution, grain size, grain boundary density, and texture changes were performed by X-ray diffraction, scanning electron microscopy, and electron backscatter diffraction. The fusion zone (FZ) comprises equiaxed cellular crystals, and a fine ~20 μm-thick crystal layer forms in the transition zone (TZ) between the FZ and heat affected zone (HAZ). The HAZ closely resembles the base material (BM), retaining the original rolling microstructure. Mechanical property testing shows that the fine-grained layer in the TZ exhibits the highest nanohardness, with the FZ corresponding to the lowest microhardness. The welded-joint sample has lower yield strength, ultimate tensile strength, and elongation after fracture than the BM. These reductions of mechanical properties are primarily influenced by the grain size and distribution of the precipitated phases.
Keywords: 5B70 aluminum alloy; vacuum electron beam welding; crystal structure; nanohardness; tensile properties

1 Introduction

Aluminum alloys are widely employed in the aerospace industry owing to their high specific strength, excellent formability, low density, and good weldability [1−3]. Research into their application in various structures is a prominent and active area [4−6]. In manufacturing aluminum alloy structural components, the joining process is critical for achieving optimal mechanical properties. Typically, conventional arc-welding techniques, such as melt inert-gas (MIG) welding and tungsten inert-gas (TIG) welding, are employed for this purpose [7,8]. However, arc-welded aluminum alloy joints often suffer from poor formability owing to their low energy density, unstable arc plasma, and extensive heat-affected zones (HAZs) as well as the formation of some defects such as pores [9−11]. Several advanced welding techniques, such as laser beam welding, electron beam welding (EBW), laser–MIG hybrid welding, and friction stir welding, have been developed to achieve high-quality welds. These methods, particularly solid-state friction stir welding, help reduce welding defects and enhance the mechanical properties of welded joints [12−17].

Corresponding author: *Guo JIN, Tel: +86-451-82518767, E-mail: jinjg721@163.com;
**Li-hong DONG, Tel: +86-10-71719584, E-mail: lihong.dong@126.com
https://doi.org/10.1016/S1003-6326(25)66972-X
Received 2 September 2024; accepted 4 March 2025

EBW is a modern high energy welding technique [18]. In EBW, the electron beam generated by the involved electron gun enters the work chamber, with electrons moving at a speed up to 200 km/s. This high-energy, concentrated electron beam, which can reach up to 10−12 W/mm^2, bombards and melts the involved sample in a vacuum. Energy transfer occurs through heat conduction on the workpiece surface. This method generally does not require a filler material [19]. By modifying the operating mode of the electron beam and electron gun whether using an oscillating or a stationary beam the amount of heat applied to the connecting components can be finely tuned across a broad range [20,21]. In EBW, the small spot size, large depth-to-width ratio, and concentrated welding heat input result in a small TZ and HAZ as well as low residual stress in the joint. In addition, the vacuum conditions used in EBW prevent the formation of oxides in the weld [22,23].

EBW is a promising welding technology owing to its benefits such as low heat input, high energy density, and precise control over the welding process [24]. These characteristics help alleviate many problems associated with traditional fusion-welding methods, such as hot cracking and alloy element loss [25,26]. FUJII et al [27] described pore formation during EBW of 2219 aluminum alloy and reported that EBW produced few pores than TIG welding. RAO et al [28] studied the EBW of 2219-T87 alloy and compared it with the results corresponding to TIG welding. The EBW joints had 42% higher strength than TIG-welded joints. This enhancement is attributed to the uniform distribution of Cu in the matrix, whereas TIG-welded joints show Cu segregation at the grain boundaries. HAYAT [29] used EBW on 7075-T6 alloy with currents of 20 and 25 mA. When the current of 25 mA was applied, the TZ exhibited high hardness and tensile strength. This is attributed to the formation of brittle intermetallic compounds in the TZ of the welded part.

The properties of welded joints are primarily influenced by the solidification structure resulting from the complex heat transfer during the molten pool's solidification. Understanding the micro-structural evolution mechanism is crucial to achieve excellent mechanical properties for welded joints. The 5B70 aluminum alloy, an advanced aerospace material, requires welding for connecting large structural components. However, research on the microstructure and properties of vacuum electron beam welded 5B70 aluminum alloy joints has not been reported. To fill this gap, the micromorphology and microstructure of 5B70 aluminum alloy joints produced by vacuum EBW were examined herein using various characterization techniques. The study focused on the microstructure, phase composition, grain size, and grain boundary characteristics of the welded joint. In addition, the effects of these microstructural features on the mechanical properties of the weld, such as microhardness, nanoscale properties, and tensile strength, were investigated. Overall, this research offers valuable insights and guidance for the application of vacuum EBW to produce 5B70 aluminum alloy joints.

2 Experimental

2.1 Materials and welding procedure

Figure 1 presents the sheet specification and welding process diagram for 5B70 aluminum alloy, along with the tensile sample and samples to be characterized. The chemical composition of the 5B70 aluminum alloy was analyzed using an inductively coupled plasma spectrometer, as listed in Table 1.

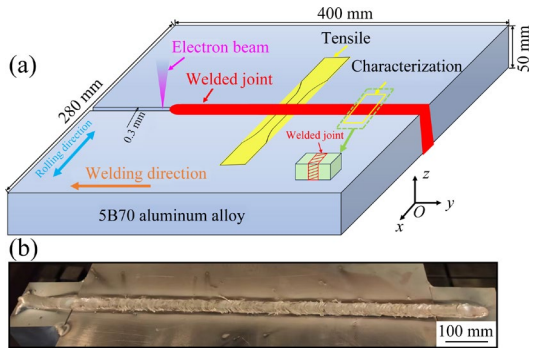

Fig. 1 Schematic of welding setup (a), and micro-morphology of welded joint (b)

Table 1 Chemical composition of aluminum alloy (wt.%)

Mg	Sc	Zr	Mn	Fe	Si	Ti	Zn	Cu	Al
5.85	0.21	0.10	0.32	0.10	0.04	0.03	0.01	0.005	Bal.

Welding was performed using EBW equipment (Model GENOVA 98, France Megmeet). Before welding, the surfaces were sanded with SiC sandpaper and cleaned with acetone to remove potential sources of weld metal porosity. To minimize the risk of welding cracks, the aluminum

alloy plates were preheated before welding. Butt welding was performed under vacuum conditions of 66.5 Pa, with an acceleration voltage, a welding current, and a focusing current of 60 kV, 210 mA, and 1.955 A, respectively. The welding speed was set as 300 mm/min, and the distance between the electron beam gun and aluminum alloy surface was 360 mm. The beam axis of the EBW device was vertically oriented, and welding was performed in a flat position. Figure 1(b) shows a photograph of the front side of the EBW joint. The surface of the welded joint is rough, exhibiting a fish-scale appearance, but is well formed with no visible porosities or cracks.

2.2 Experimental procedure

For microstructure characterization, samples were sequentially ground with SiC sandpaper, polished using a 0.5 μm diamond suspension, and then etched with Keller's reagent, which comprises 5 mL HNO_3, 10 mL HF, and 85 mL H_2O. The microstructure of the welded joint was examined using a metallographic microscope. In addition, scanning electron microscopy (SEM) equipped with energy dispersive X-ray spectrometry (EDS) was used to observe the microstructure of sample and analyze the chemical composition at various locations. An electron microscope equipped with an electron backscatter diffraction (EBSD) probe was employed to analyze the microstructural evolution of the sample, with a scanning step size of 0.4 μm. The AztecCrystal software extracted the following data from EBSD analysis: average grain size, high- and low-angle grain boundaries (HAGB and LAGBs, respectively), local-orientation difference map (kernel average misorientation (KAM) map), grain boundary distribution map, and microtexture in the form of a pole figure (PF).

Microhardness was measured using a micro-hardness tester, with Vickers hardness ($HV_{0.1}$) recorded under a 100 g load and 15 s loading time. Testing was performed from the center of the weld joint outward to the HAZ and BM, with measurements taken every 200 μm. To ensure data reliability, three longitudinal points were tested with 200 μm intervals, and the results were averaged. Nanoscale properties were assessed using a nanoindentation testing machine at room temperature. A Berkovich triangular pyramid diamond indenter was used for nanoindentation, with a maximum load of 14 mN and loading time of 10 s. The elastic modulus (E), nanohardness (H), and plasticity factor (η) were derived from the load–displacement curves of the welded joint, such as the FZ, TZ, HAZ, and BM.

Static tensile tests were performed using an MTS809 servo-hydraulic testing machine at room temperature, with a constant displacement rate of 1 mm/min. The tensile test samples were prepared according to the dimensions presented in Fig. 2. Three sets of samples were tested to ensure data reliability. The average values of yield strength (YS), ultimate tensile strength (UTS), and elongation after fracture were determined, and the fracture morphology was examined using SEM.

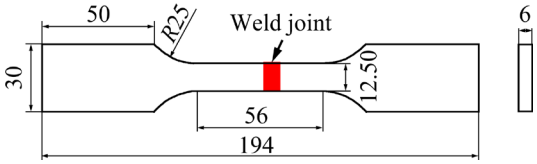

Fig. 2 Dimensions of tensile specimen (unit: mm)

3 Results and discussion

3.1 Metallographic morphology

Figure 3 shows the metallographic morphology of the 5B70 aluminum alloy joint welded using vacuum EBW, viewed in the cross-sectional direction (A−B plane in Fig. 3). There are no defects, such as pores or cracks. The welded joint comprises four zones: the weld FZ, TZ, HAZ, and BM. There is a strong metallurgical bond between the FZ and BM. The phase composition and microstructural evolution in each region of the weld joint were further analyzed by XRD, SEM, and EBSD.

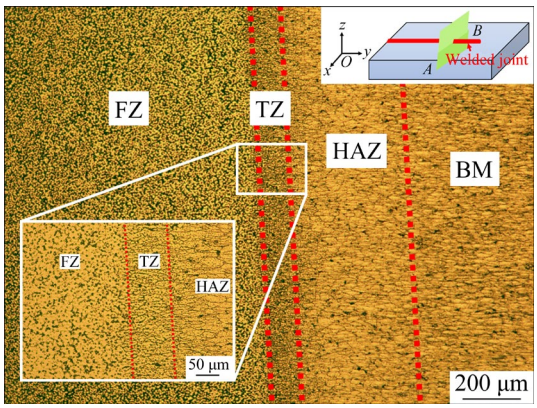

Fig. 3 Metallographic morphology of welded joint

3.2 Phase composition

Figure 4 shows the phase composition of different regions in the 5B70 aluminum alloy joint welded using vacuum EBW. XRD patterns show that the FZ, HAZ, and BM regions predominantly comprise the α(Al), Al_6(Fe,Mn), and Al_3(Sc,Zr) phases. Notably, the diffraction peak at 81.68° is absent in the FZ diffraction pattern, which may be attributed to a reduction owing to phase dissolution during vacuum EBW [30].

3.3 SEM morphology

To further examine the microstructure of the 5B70 aluminum alloy joint welded using vacuum EBW, SEM characterization was performed in the cross-sectional direction (Fig. 5). There are no microscopic defects in the FZ, TZ, and HAZ (Figs. 5(a−c)).

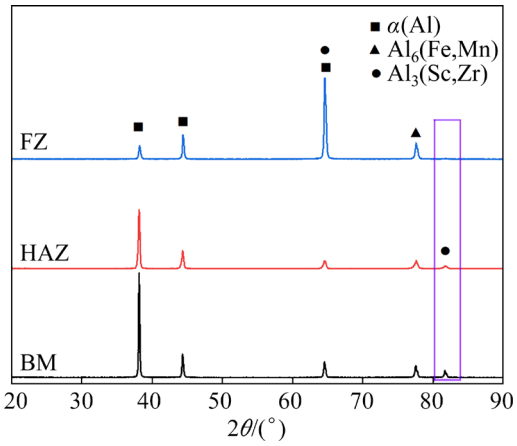

Fig. 4 XRD patterns of welded joint

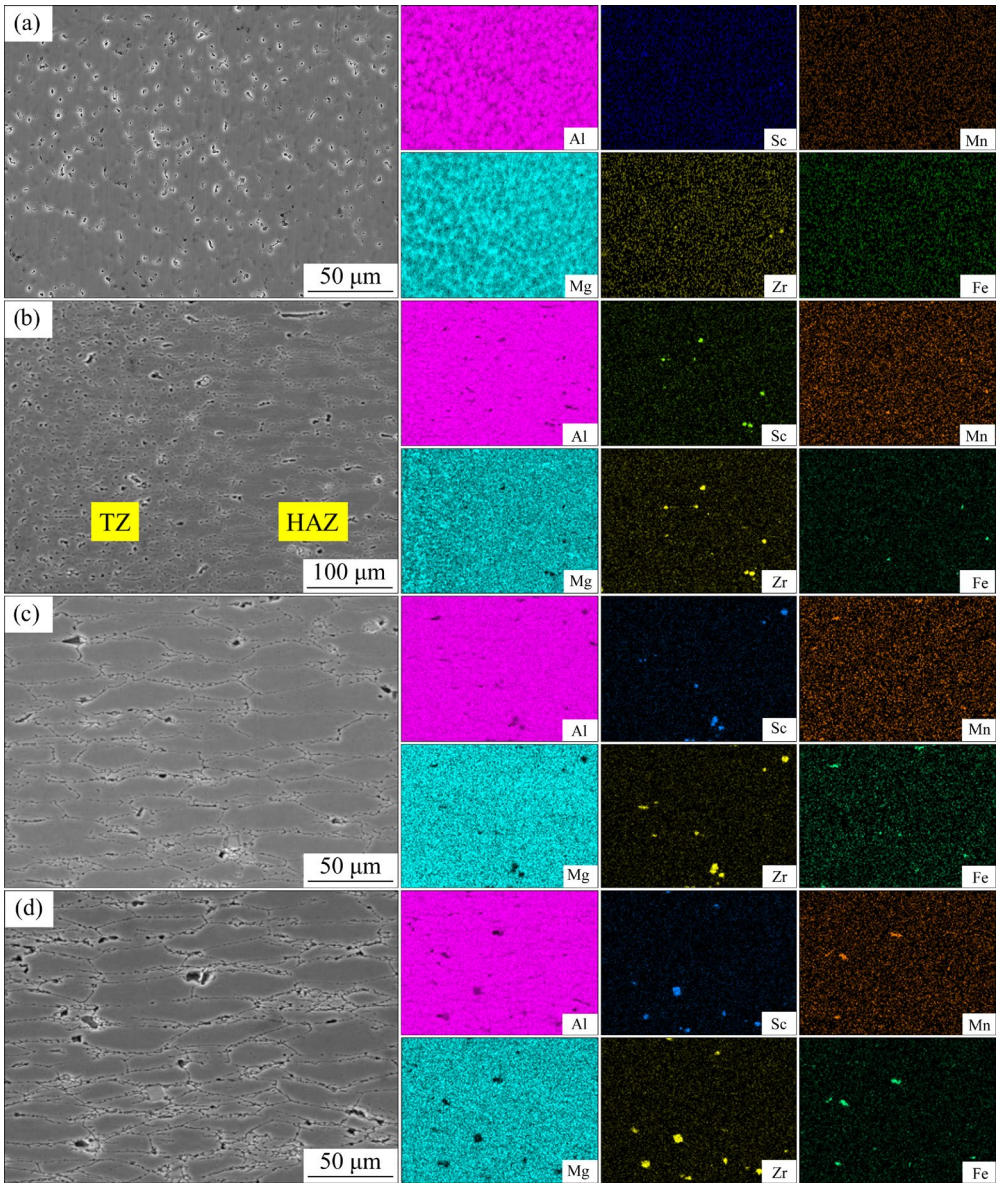

Fig. 5 SEM images and EDS mapping of welded joint: (a) FZ; (b) TZ; (c) HAZ; (d) BM

The weld zone displays a typical cold structure. During EBW, the aluminum alloy experiences rapid heating, melting, and solidification in accordance with solidification theory and crystallographic principles [31]. Grain size and morphology are influenced by the ratio of the temperature gradient (G) to the solidification rate (R) during solidification. With increasing G/R ratio, the supercooling degree of the weld center also increases, promoting nucleation. This leads to simultaneous grain nucleation. In addition, in the FZ, heat dissipation becomes less directional, allowing nucleation to grow without preferred directionality, resulting in nearly uniform growth rates in all directions. Consequently, the microstructure of the FZ is characterized by equiaxed cellular crystals (Fig. 5(a)) with no distinct orientation trend. This observation aligns with the findings of HOSSEINI et al [32]. Figure 5(b) shows the TZ microstructure. The fusion between the FZ and BM is effective, resulting in a smooth and continuous interface that indicates a strong metallurgical bond. The HAZ and BM retain their original rolling structure characteristics. EDS mapping shows that the FZ has low content and small size of precipitated phases, primarily comprising Al_3(Sc,Zr). In contrast, the precipitated phases in the HAZ and BM predominantly include Al_6(Fe,Mn) and Al_3(Sc,Zr).

3.4 Crystal structure evolution

EBSD microstructure analysis shows considerable variations in heat input across different regions of vacuum electron beam welded joints, leading to difference and inhomogeneity in the microstructure of each area.

The inverse PF (IPF) for the FZ (Fig. 6(a)) aligns with the SEM microstructure (Fig. 5(a)), both showing equiaxed cell crystals with an average grain size of 8.66 μm. In the BM, grains are deformed along the RD direction with a preferred orientation in the (111) direction; this preferentiality is entirely lost in the FZ owing to the effects of welding thermal cycling. Figure 6(c) shows the microstructure of the TZ. A fine crystal layer approximately 20 μm in width forms in the TZ between the FZ and HAZ. This formation is primarily attributed to the accumulation of alloying elements such as Mg, Fe, Mn, Sc, and Zr near the fusion line (Fig. 5(b)) driven by thermal buoyancy and Marangoni convection. During solidification, the concentration of solute elements in the liquid metal increases owing to the enrichment of alloying elements at the solid−liquid interface, leading to greater subcooling. The rapid solidification rate near the fusion line of the BM creates dynamic conditions conducive to the development of a zone of equiaxed, fine crystals. The TZ is connected to the HAZ, where G is high. This causes the TZ to rapidly solidify from the edges toward the center, with the nucleation rate of the grains exceeding the growth rate, leading to the formation of fine grains. The lattice mismatch between the Al_3(Sc,Zr) phase (lattice constant: 0.409 nm) and the Al matrix (lattice constant: 0.405 nm) is less than 5%, and the high thermal stability of the Al_3(Sc,Zr) phase satisfies the structural and dimensional requirements for heterogeneous nucleation cores [33−35]. The average grain size in the equiaxed fine crystal zone is 4.08 μm. Figures 6(e) and (g) show the morphology of the HAZ and BM, respectively.

There is no notable difference between the HAZ and BM, with the HAZ retaining some of the rolling structure. However, owing to the heat input during welding, some grains in the HAZ grow. The average grain sizes in the HAZ and BM are 7.21 and 4.53 μm, respectively.

Figure 7 shows the distribution of KAM and grain orientation spreading (GOS) across different regions of the welded joint. As shown in Figs. 7(a, b), (d, e), (g, h), and (j, k), the KAM value gradually increases from the FZ to the HAZ and then to the BM, with the BM exhibiting the highest KAM value of 0.74°. This variation in local orientation reflects differences in grain deformation and dislocation density distribution. Both the HAZ and BM exhibit higher deformation degrees and greater dislocation densities than the FZ. The microstructure of the FZ primarily comprises equiaxed cell crystals with minimal residual deformation, resulting in a low KAM value. In contrast, the welding heat input reduces the deformation of the BM; however, the BM, unaffected by welding, retains its original 5B70 aluminum alloy rolling microstructure and shows the highest deformation degree, leading to the highest KAM value.

In the FZ, LAGBs (<10°) and HAGBs (>10°) are present in proportions of 3.5% and 96.5%, respectively, indicating a dominance of HAGBs. In

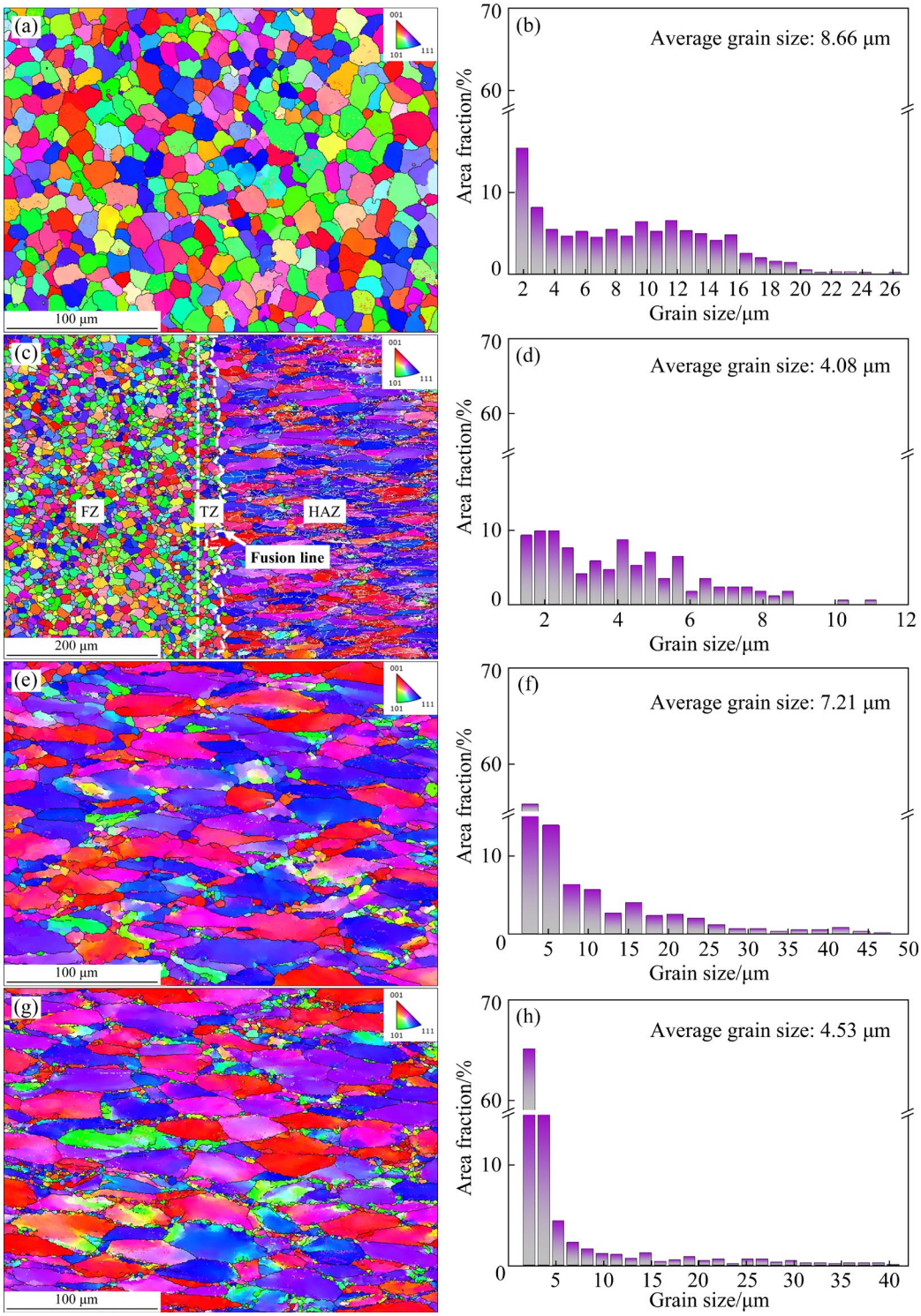

Fig. 6 IPF morphology and grain size of welded joint: (a, b) FZ; (c, d) TZ; (e, f) HAZ; (g, h) BM

contrast, the grain orientation angles of the BM and HAZ are similar, with both regions having approximately equal proportions of HAGBs and LAGBs. This similarity is attributed to the retention of the rolled microstructure in both the BM and HAZ, leading to partial grain recrystallization and sub-grain formation, which typically results in a GOS less than 2° for the sub-grains [36]. Thus, the proportion of LAGBs is considerably higher in the BM and HAZ than that in the FZ. Furthermore, FEI et al [37] and WAN et al [38] reported that HAGBs are effective in inhibiting crack growth and the abundance of HAGBs in the FZ enhances its mechanical properties.

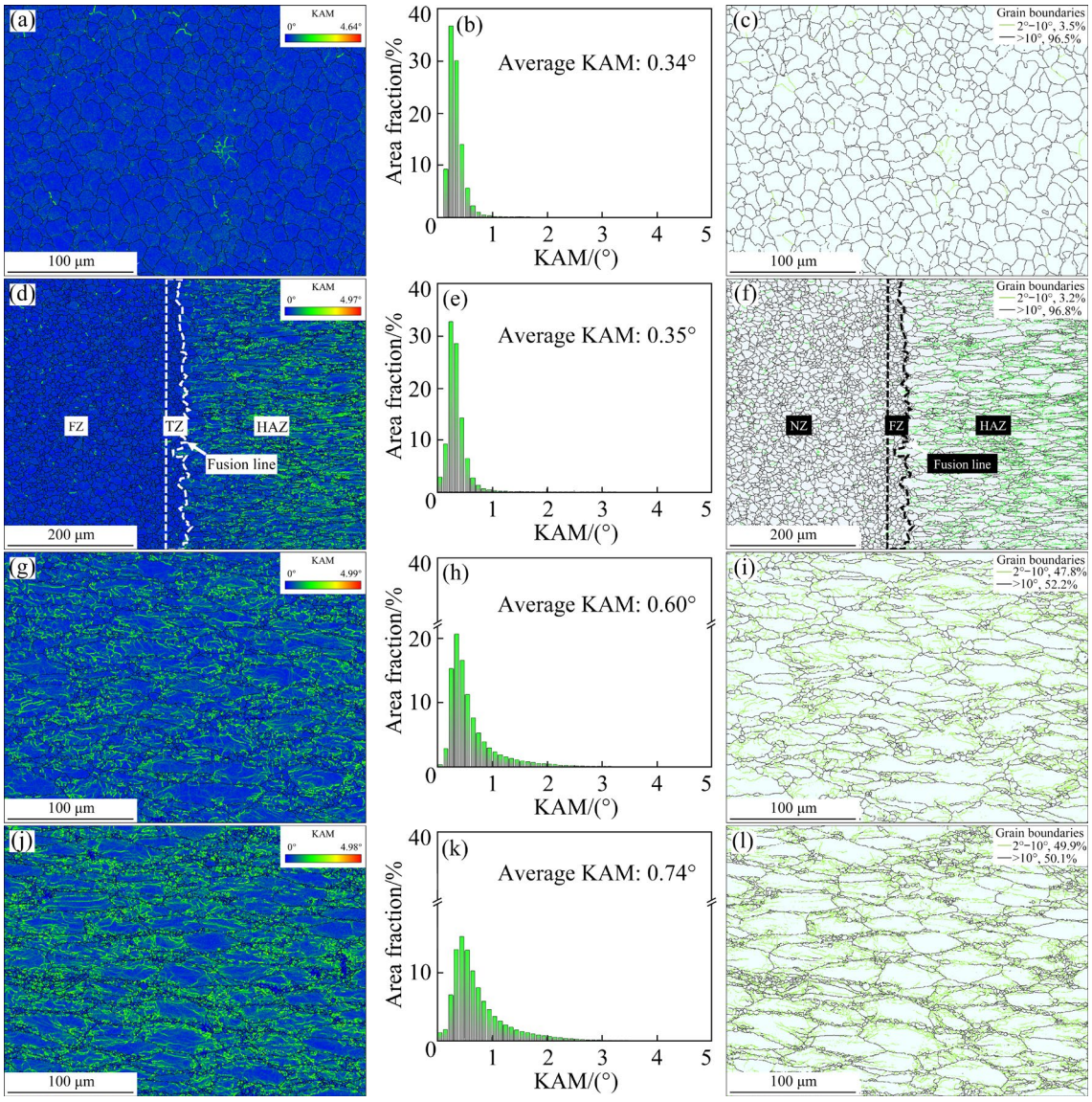

Fig. 7 KAM and GOS diagrams of welded joint: (a−c) FZ; (d−f) TZ; (g−i) HAZ; (j−l) BM

3.5 Texture evolution

The EBSD results provide insights into the changes in texture structure across different regions. Figure 8 shows the polar figures for various areas of the welded joint. The maximum polar densities are 5.33 and 5.43 for the HAZ and BM, respectively, indicating a strong preferred orientation. After EBW, the maximum polar density in the FZ region decreases to 2.20 and the distinct texture observed in the BM is no longer present. This indicates that the grain orientation in the FZ becomes random, with no preferred texture.

Similar findings have been reported in other studies on EBW of aluminum alloys. CHEN et al [39] studied the texture initially comprising a mixture of brass {110}⟨112⟩ and cubic {001}⟨110⟩, which provides high strength in the BM. However, in the FZ, there was no preferred orientation owing to free grain growth. In addition, polar densities decreased after welding, and similar results have been reported for other welding materials. WU et al [40] studied commercially pure titanium and observed that the BM exhibited a strong rolling texture, which decreased in the FZ. The presence of columnar grains in the FZ likely introduced a solidification texture, leading to a change in the overall texture.

3.6 Microhardness

Figure 9 presents the microhardness test results for the vacuum electron beam welded joint of 5B70 aluminum alloy, showing a symmetrical distribution. Microhardness progressively increases from the FZ

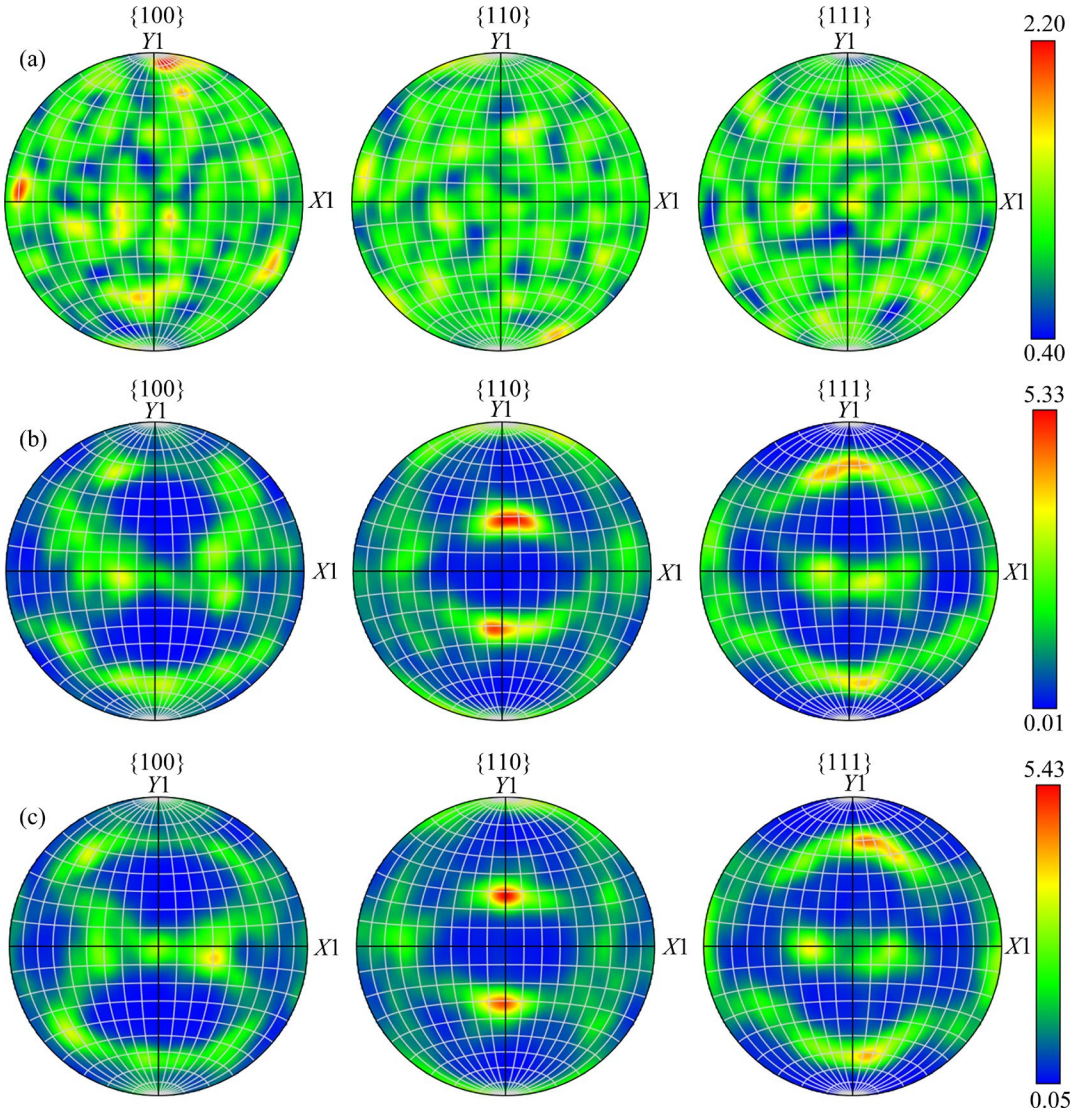

Fig. 8 Pole figure of welded joint: (a) FZ; (b) HAZ; (c) BM

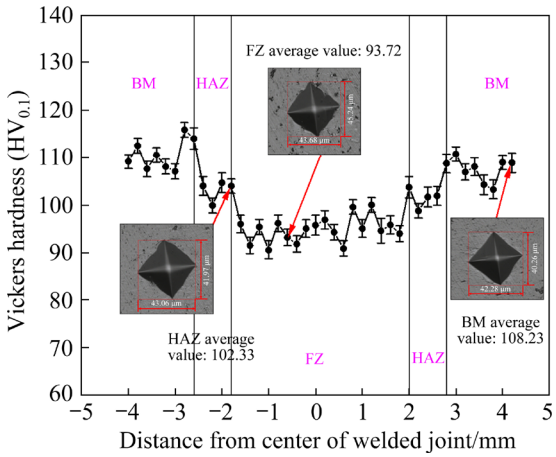

Fig. 9 Distribution of microhardness in welded joint

to the HAZ and BM regions. The average microhardnesses are $HV_{0.1}$ 93.72, $HV_{0.1}$ 102.33, and $HV_{0.1}$ 108.23 for the FZ, HAZ, and BM, respectively. The microhardness of the FZ is ~86.59% that of the BM.

The mechanical properties of light alloys used in aerospace are considerably influenced by the quantity and distribution of precipitated phases. ZHANG et al [41] investigated laser welding on 2060 aluminum alloy, and reported that the average microhardness of the FZ was the lowest, approximately 70% that of the BM. FARAJI et al [42] showed that in Nd laser−TIG hybrid welding, the average microhardness of the FZ in 2198 aluminum alloy was 62% that of the BM. The high heat input from welding caused a considerable reduction in microhardness. DING et al [43] studied the TIG welding of 2219 aluminum alloy and found that the microhardness of the FZ was only 44.6% that of the BM. Notably, during Vickers microhardness test, the

narrow width of the TZ made it difficult for the relatively large indenter to accurately measure the TZ microhardness. Therefore, nanoindentation tests were performed in various areas of the welded joint to obtain accurate measurements.

The analysis of microhardness results and their influencing mechanisms reveals two primary factors contributing to the observed results. First, the FZ microstructure comprises equiaxed cell crystals with an average grain size of 8.66 μm, considerably larger than that in the HAZ and BM. The smaller grains in the HAZ and BM result in a more pronounced grain boundary-strengthening effect. Second, the content of precipitated phases affects the material's plasticity and toughness [44]. A statistical analysis of the precipitated-phase content in different areas of the welded joint provides further insights into these effects. Figure 10 shows that the precipitated-phase contents are 2%, 2.7%, and 3.6% in the FZ, HAZ, and BM, respectively. The lowest content in the FZ is attributed to the high peak temperature at the center of the weld, which causes precipitated-phase dissolution. In addition, rapid cooling reduces the precipitation time of these phases in the material, further decreasing their content [45]. Furthermore, the FZ precipitated-phase distribution reveals that the precipitated phase is unevenly distributed with noticeable agglomeration. In contrast, the precipitates in the HAZ and BM are more uniformly distributed. However, in the HAZ, precipitates grow owing to the welding heat input, resulting in slightly lower microhardness compared with that corresponding to the BM.

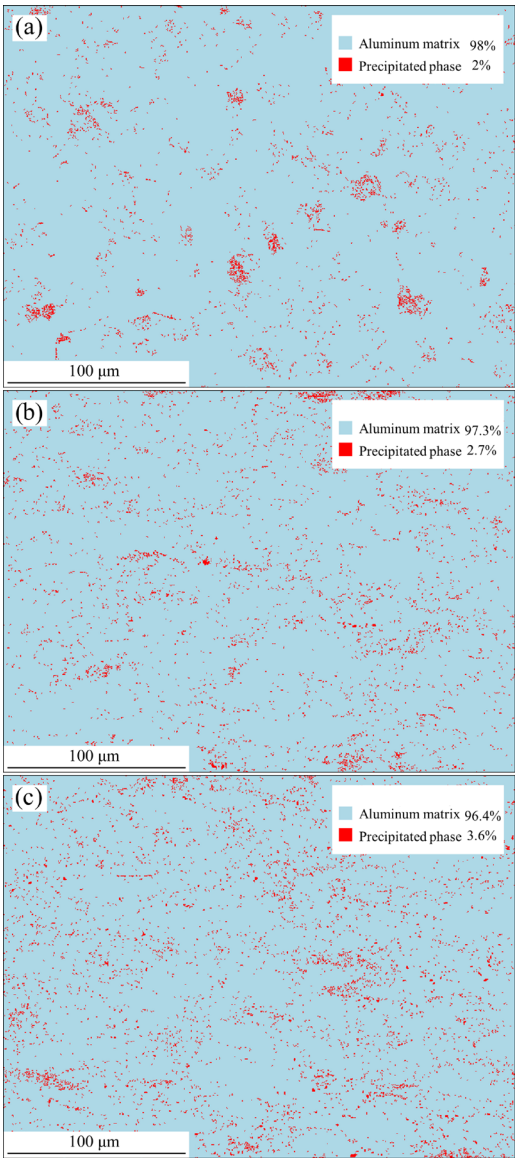

Fig. 10 Distribution of precipitated phases of welded joint: (a) FZ; (b) HAZ; (c) BM

3.7 Nanoindentation test results

Nanoindentation, a technique for nanoscale characterization, is a powerful tool for assessing the local mechanical properties of welded joints [46]. This method is particularly well suited for investigating how microstructural changes, such as variations in grain size, precipitated phases, and phase transformations, affect the overall mechanical behavior of welded joints.

Nanoindentation tests were performed across various regions of the vacuum electron beam-welded 5B70 aluminum alloy joint. The load−displacement data were analyzed using the method developed by OLIVER and PHARR [47]. The method accounts for the elastic recovery of surface upon unloading. Figure 11(a) shows the load–displacement curves for different regions of the welded joint (FZ, TZ, HAZ, and BM). As shown, at 14 mN of load, the indentation depth in the TZ is the lowest at 599.32 nm, whereas the FZ exhibits the highest indentation depth at 783.12 nm. The depths for the HAZ and BM are 689.31 and 657.48 nm, respectively. This indicates that under 14 mN of load, the nanohardness of the TZ region is the highest.

Figure 11(b) shows the elastic modulus (E), hardness (H), and plasticity factor (η) across different regions of the welded joint under 14 mN of load. The results indicate that the TZ exhibits the highest nanohardness at 1.57 GPa, whereas the FZ shows the lowest at 1.015 GPa. The hardnesses for the HAZ and BM are 1.243 and 1.319 GPa,

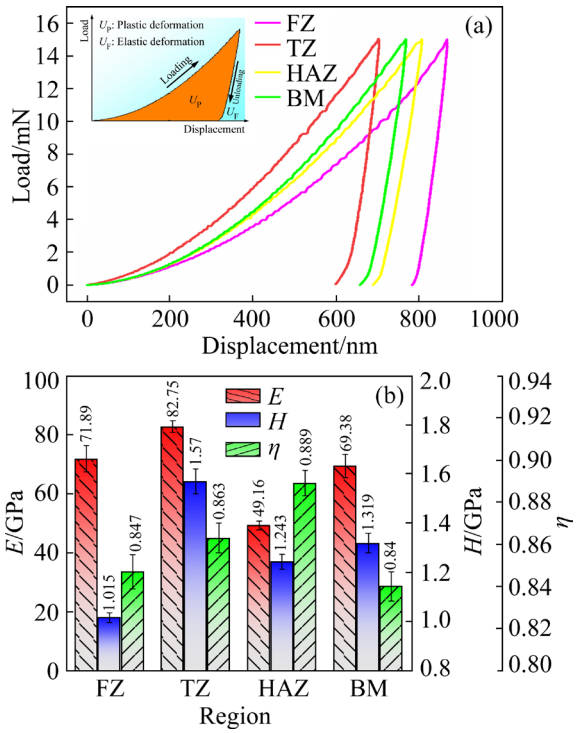

Fig. 11 Nanoindentation test results of welded joint: (a) Load–displacement curve; (b) Elastic modulus (E), nanohardness (H), and plasticity factor (η)

respectively. These findings from the nanoindentation tests align with the microhardness test results. In particular, the hardnesses of the HAZ and FZ are lower than that of the BM, with the reduced hardness in the HAZ attributed to grain growth caused by the welding heat input. The decrease of hardness in the FZ is primarily attributed to precipitated-phase dissolution. Variations in indentation depth, nanohardness, and elastic modulus across different regions of the welded joint reflect differences in plastic deformation and mechanical response. The plastic factor (η), defined as the ratio of the plastic deformation energy (U_p) to the total deformation energy (U_T), as shown in Formulas (1) and (2), measures the material's resistance to plastic deformation. A smaller η indicates better resistance to plastic deformation. The low η for BM and FZ further indicate their high resistance to plastic deformation.

$$\eta=\frac{U_p}{U_T} \tag{1}$$

$$U_T=U_p+U_E \tag{2}$$

where U_E is the elastic deformation energy.

3.8 Tensile test result

Figure 12 presents the results of static tensile tests performed on the 5B70 aluminum alloy BM and electron beam welded joint samples. Each sample group was tested thrice, with fractures consistently occurring in the FZ and TZ of the welded joints. Both the YS and UTS of the welded-joint samples are considerably lower than those of the BM. In particular, the YS of the welded-joint samples is 24.63% (242.33 MPa) lower than that of the BM (321.5 MPa). In addition, tensile elongation considerably decreased, with the BM exhibiting 16.66% elongation compared with 10.01% for the welded-joint sample. This represents a decrease of 39.92%, indicating that the weld has a considerable influence on the elongation after fracture.

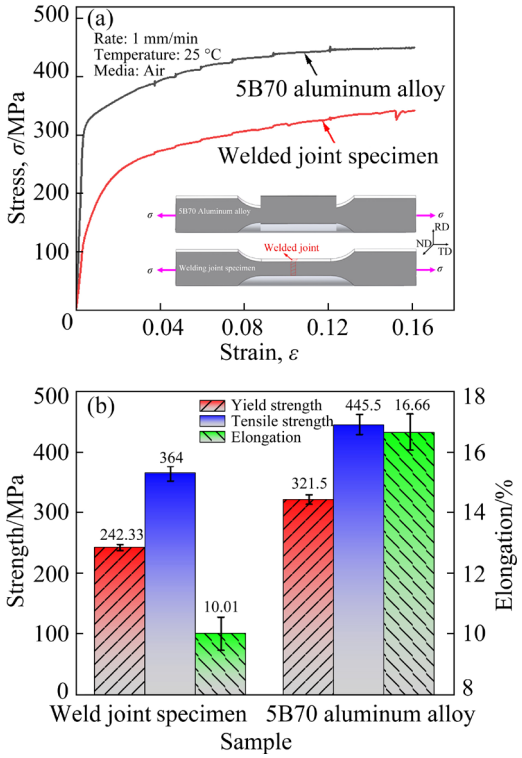

Fig. 12 Tensile test results of 5B70 aluminum alloy and welded joints: (a) Tensile stress–strain curve; (b) Tensile property

One factor contributing to the reduction in tensile strength is the dissolution of precipitated-phase particles in the weld. These particles, which are present in the BM alloy, are crucial in strengthening the material. During welding, high temperatures cause these particles to dissolve, thus reducing the overall joint strength. This effect is illustrated by the distribution of precipitated phases in the FZ (Fig. 10(a)) [48]. The development of a

coarse crystal structure in the FZ during welding further reduces the welded joint strength. According to Hall−Petch relation, as expressed in Formula (3), YS of the alloy is inversely related to the average grain size [49]. In addition, the loss of elements due to evaporation during welding contributes to the reduced tensile strength. The evaporation rate of metals is described by the Hertz−Knudsen−Langmuir equation. During EBW, the mass loss is driven by the difference in pressure between the vapor pressure of the metal and the ambient pressure in the vacuum chamber [50,51]. ZHAN et al [52] also reported similar findings; in the weld of 6061 aluminum alloy, severe burning loss of magnesium and the formation of pores resulted in a tensile strength considerably lower than that of the BM, with elongation ~2%. Furthermore, rapid cooling during welding creates a high thermal gradient, leading to the development of residual stresses in the joint. These residual stresses can act as internal forces that weaken the material, further reducing its strength [53,54].

$$R_{p0.2}=R_{pure}+kd^{-1/2} \quad (3)$$

where $R_{p0.2}$ is the YS of alloy, R_{pure} is the YS of pure metal, k is a constant, and d is the average grain size.

The elongation of the welded-joint sample is 39.92% lower than that of the BM, possibly owing to the weld zone, which leads to uneven strain distribution during deformation and affects the overall elongation of the joint. In addition, the nonuniform grain morphology in the welded joint, with a larger average grain size compared with that of the BM, likely contributes to the reduced tensile elongation. Notably, fractures occur in the welded joint region rather than the BM region, which can be attributed to the fine grain structure and dislocation accumulation in the weld. Moreover, the high precipitated-phase content in the BM helps bind dislocations, impedes their movement, and contributes to dislocation accumulation. When the metal deforms, the dislocation requires more energy to cut through the strengthening phase, thus increasing the material strength [48].

The fracture morphology of the 5B70 aluminum alloy electron beam-welded joint was examined and analyzed using SEM to understand the fracture mode and characteristics. Figure 13(a) shows the fracture morphology, which shows typical ductile fracture behavior. The fracture surface features several distinct characteristics, such as dimples, secondary-phase particles, and tear ridges. Figure 13(b) shows a magnified view of the red box in Fig. 13(a), revealing that the dimples are round or

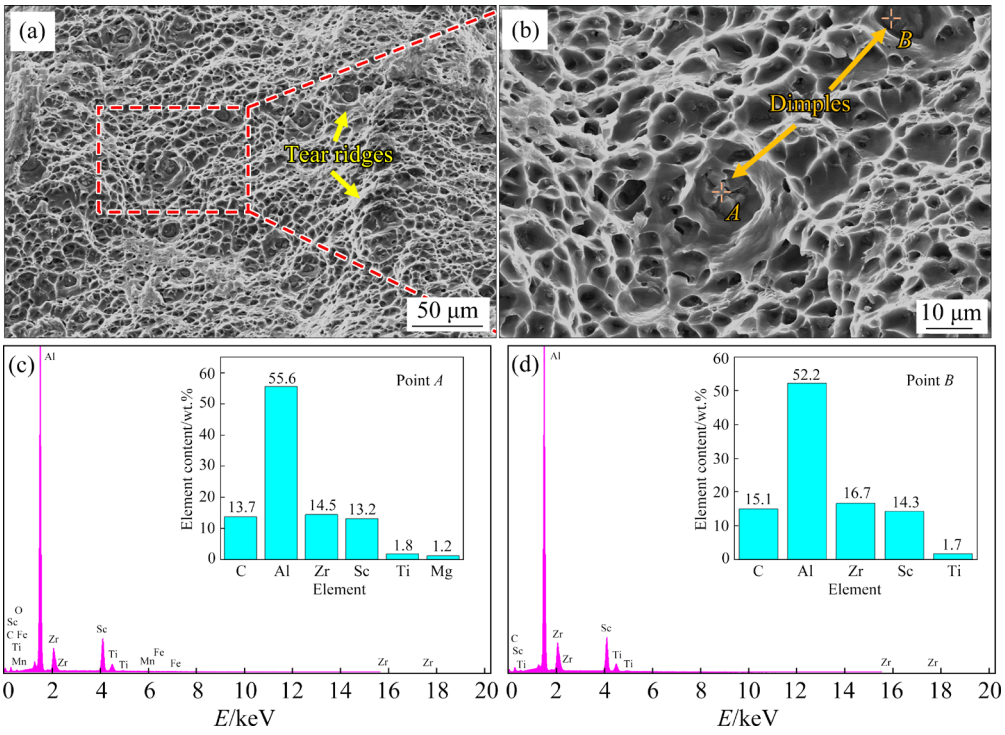

Fig. 13 Tensile-fracture morphology (a, b) of welded joint and corresponding EDS analysis (c, d): (a) Fractured surface; (b) Magnified image of area indicated in (a); (c) EDS analysis at Point *A*; (d) EDS analysis at Point *B*

oval and vary in size, indicating plastic deformation and energy absorption during the fracture process, with a predominant intergranular fracture mode. The presence of defects or areas of stress concentration can cause strain localization, leading to the formation of small dimples. The presence of these dimples indicates that the material can undergo considerable plastic deformation before failure [55]. Second-phase particles at the base of the dimples act as barriers to crack growth, contributing to the material's fracture resistance [56]. EDS analysis of the areas marked *A* and *B* in Fig. 13(b) reveals that these second-phase particles are primarily Al_3(Sc,Zr) phases. In addition, tear ridges observed along the fracture surface indicate material tearing and separation. The presence of dimples, second-phase particles, and tear ridges on the fracture surface of the 5B70 aluminum alloy electron beam welded joint collectively demonstrates its ductile fracture behavior.

4 Conclusions

(1) The joint comprises four areas: FZ, TZ, HAZ, and BM. The XRD phase analysis reveals that each region of the welded joint contains the α(Al), Al_6(Fe, Mn), and Al_3(Sc, Zr) phases.

(2) The FZ has equiaxed cellular crystals, the TZ contains a fine crystal layer of ~20 μm in thickness, and the HAZ retains the rolled microstructure of the BM, although with larger grain sizes.

(3) The microhardness indicates a decrease from the BM to the HAZ and further to the FZ, primarily due to variations in grain size and precipitated-phase distribution. Nanoindentation testing reveals that the TZ exhibits the highest nanohardness, whereas η is larger for both the TZ and HAZ, indicating lower resistance to plastic deformation.

(4) Compared with the BM, the YS of the welded-joint specimens are reduced by 24.63% and the elongation after fracture decreases by 39.92%. The tensile fracture morphology is characteristic of ductile fracture.

CRediT authorship contribution statement

Yu-peng ZHANG: Data curation, Methodology, Visualization, Writing – Original draft; **Guo JIN:** Conceptualization, Supervision, Writing – Review & editing, Resources; **Li-hong DONG:** Conceptualization, Supervision, Writing – Review & editing, Resources; **Xiu-fang CUI:** Formal analysis, Resources; **Chong GAO:** Supervision, Methodology, Validation; **Xiang-yu XIE:** Supervision, Formal analysis, Validation; **Yue-lan DI:** Investigation, Supervision, Writing – Review & editing; **Wei-ling GUO:** Supervision, Validation; **Ya-ya SONG:** Data curation, Formal analysis; **Wen-jing SHI:** Writing – Review & editing; **Ru-chuan ZENG:** Methodology; **Ning HUANG:** Methodology, Formal analysis.

Declaration of competing interest

The authors declare that they have no known competing financial interests or personal relationships that could have appeared to influence the work reported in this paper.

Acknowledgments

This work was supported by the National Natural Science Foundation of China (Nos. 52175206, 52205187, 52130509), and the Science and Technology Planning Project of Guizhou Province, China (No. ZK[2022]013).

References

[1] ÇAM G, İPEKOĞLU G. Recent developments in joining of aluminum alloys [J]. The International Journal of Advanced Manufacturing Technology, 2017, 91(5/6/7/8): 1851−1866.

[2] KASHAEV N, VENTZKE V, ÇAM G. Prospects of laser beam welding and friction stir welding processes for aluminum airframe structural applications [J]. Journal of Manufacturing Processes, 2018, 36: 571−600.

[3] AHMED M M Z, SELEMAN M M E, FYDRYCH D, ÇAM G. Friction stir welding of aluminum in the aerospace industry: The current progress and state-of-the-art review [J]. Materials, 2023, 16(8): 2971.

[4] WANG Guo-qing, ZHAO Yan-hua, HAO Yun-fei. Friction stir welding of high-strength aerospace aluminum alloy and application in rocket tank manufacturing [J]. Journal of Materials Science & Technology, 2018, 34(1): 73−91.

[5] LIPIŃSKA M, PIXNER F, SZACHOGŁUCHOWICZ I, MITTERMAYR F, GRENGG C, ENZINGER N, LEWANDOWSKA M. Application of electron beam welding technique for joining coarse-grained and ultrafine-grained plates from Al−Mg−Si alloy [J]. Journal of Manufacturing Processes, 2023, 104: 28−43.

[6] YANG Jian-lei, SONG Jiang-hao, PAN Jin-qi, WANG Xiao-bo, ZHOU Li, SUN Guang-da, ZHANG Wen-cong, JIAO Xue-yan. Microstructure evolution and strengthening mechanisms of electron beam welded 2219 aluminum alloy plate after hot spinning and heat treatment [J]. Journal of Materials Research and Technology, 2024, 28: 411−419.

[7] CUI Shu-wan, TIAN Fu-yuan, MA Rong, YU Yun-he, XU Lei.

Study on the morphology, microstructure, and properties of 6082-T6 aluminum alloy joints in MIG welding [J]. Metals, 2023, 13(7): 1245.

[8] HABBA M I A, ALSALEH N A, BADRAN T E, SELEMAN M M, ATAYA S, EL-NIKHAILY A E, ABDUL-LATIF A, AHMED M M Z. Comparative study of FSW, MIG, and TIG welding of AA5083-H111 based on the evaluation of welded joints and economic aspect [J]. Materials, 2023, 16(14): 5124.

[9] İPEKOĞLU G, ÇAM G. Formation of weld defects in cold metal transfer arc welded 7075-T6 plates and its effect on joint performance [J]. IOP Conference Series: Materials Science and Engineering, 2019, 629: 012007.

[10] ÇAM G. Prospects of producing aluminum parts by wire arc additive manufacturing (WAAM) [J]. Materials Today: Proceedings, 2022, 62: 77−85.

[11] ÇAM G, GÜNEN A. Challenges and opportunities in the production of magnesium parts by directed energy deposition processes [J]. Journal of Magnesium and Alloys, 2024, 12(5): 1663−1686.

[12] CHEN Shuai, CHENG Sheng, WANG Yu, YU Ke-zhuang, LI Li, CAO Hong-zhi, MA Zheng-wei. Numerical analysis on temperature characteristics and melt flow dynamic behaviors in electron beam welding of dissimilar aluminum alloy lock-butt joint [J]. The International Journal of Advanced Manufacturing Technology, 2024, 131(7/8): 4267−4280.

[13] WEI Yi-yun, YANG Kun-ming, YIN Xue-feng, ZHAO Ya-wen, SU Bin, HE Jian-jun, SHI Tao, LU Chao, LI Rui-wen, YANG Lei, WANG Wen-yuan, YU Liang-bo, XU Qing-dong, ZHANG Peng-cheng. Micro-mechanical properties and associated strengthening mechanism of Be−Al−Ag−Si alloys fabricated by electron beam welding technique [J]. Materials Characterization, 2024, 209: 113759.

[14] YU Peng-fei, WU Chuan-song, SHI Lei. Analysis and characterization of dynamic recrystallization and grain structure evolution in friction stir welding of aluminum plates [J]. Acta Materialia, 2021, 207: 116692.

[15] KHALIQ U A, MUHAMAD M R, YUSOF F, IBRAHIM S, ISA M S M, CHEN Z, ÇAM G. A review on friction stir butt welding of aluminum with magnesium: A new insight on joining mechanisms by interfacial enhancement [J]. Journal of Materials Research and Technology, 2023, 27: 4595−4624.

[16] AHMED M M Z, SELEMAN M M E, FYDRYCH D, FYDRYCH D, ÇAM G. Review on friction stir welding of dissimilar magnesium and aluminum alloys: Scientometric analysis and strategies for achieving high-quality joints [J]. Journal of Magnesium and Alloys, 2023, 11(11): 4082−4127.

[17] TANG Yi-shuang, LI Wen-ya, ZOU Yang-fan, WANG Wei-bin, XU Ya-xin, VAIRIS A, ÇAM G. Effects of tool rotation direction on microstructure and mechanical properties of 6061 aluminum alloy joints by the synergistically double-sided friction stir welding [J]. Journal of Manufacturing Processes, 2024, 126: 109−123.

[18] WEGLOWSKI M S, BŁACHA S, PHILLIPS A. Electron beam welding−techniques and trends−Review [J]. Vacuum, 2016, 130: 72−92.

[19] ÇAM G, KOÇAK M. Microstructural and mechanical characterization of electron beam welded Al-alloy 7020 [J]. Journal of Materials Science, 2007, 42(17): 7154−7161.

[20] PUYDT Q, FLOURIOT S, RINGEVAL S, de GEUSER F, PARRY G, DESCHAMPS A. Relationship between microstructure, strength, and fracture in an Al−Zn−Mg electron beam weld: Part I: Microstructure characterization [J]. Metallurgical and Materials Transactions A, 2014, 45(13): 6129−6140.

[21] NAGAI T, KASAI R, UENO K, MOCHIZUKI M, SUGA T. Effects of metal types on residual stress in electron-beam welding joints with sheet metals [J]. ISIJ International, 2015, 55(1): 241−249.

[22] XU Ming-fang, CHEN Yu-hua, ZHANG Ti-ming, XIE Ji-lin, WANG Shan-lin, YIN Li-meng, HE Peng. Microstructure evolution and mechanical properties of wrought/wire arc additive manufactured Ti−6Al−4V joints by electron beam welding [J]. Materials Characterization, 2022, 190: 112090.

[23] TÜMER M, PIXNER F, VALLANT R, DOMITNER J, ENZINGER N. Mechanical and microstructural properties of S1100 UHSS welds obtained by EBW and MAG welding [J]. Welding in the World, 2022, 66(6): 1199−1211.

[24] XIA Hai-qing, XU Yi, YU Ying-jie, DUAN Xing-yun, ZHU Shuai, LEI Ya-ping, WANG Ao, SHI Peng-fei, FENG Mei-bing, ZHU Fang, NIE Teng-fei, TANG Jian-cheng. Numerical simulation and properties analysis of Ta10W alloy joints prepared by electron beam welding [J]. International Journal of Refractory Metals and Hard Materials, 2024, 124: 106819.

[25] ÇAM G, VENTZKE V, DOS SANTOS J F, KOÇAK M. Characterization of laser and electron beam welded Al alloys [J]. Praktische Metallography, 2000, 37(2): 59−89.

[26] ÇAM G, VENTZKE V, DOS SANTOS J F, KOÇAK M. Characterisation of electron beam welded aluminium alloys [J]. Science and Technology of Welding and Joining, 1999, 4(5): 317−323.

[27] FUJII H, UMAKOSHI H, AOKI Y, NOGI K. Bubble formation in aluminium alloy during electron beam welding [J]. Journal of Materials Processing Technology, 2004, 155: 1252−1255.

[28] RAO S R K, REDDY G M, RAO K S, KAMARAJ M, RAO K P. Reasons for superior mechanical and corrosion properties of 2219 aluminum alloy electron beam welds [J]. Materials Characterization, 2005, 55(4/5): 345−354.

[29] HAYAT F. Electron beam welding of 7075 aluminum alloy: Microstructure and fracture properties [J]. Engineering Science and Technology, 2022, 34: 101093.

[30] TANG Hao, XI Xiao-ying, GAO Chao-feng, LIU Zhong-qiang, ZHANG Jian-tao, ZHANG Wei-wen, XIAO Zhi-yu, RAO J H. Microstructure evolution and strengthening mechanisms of a high-performance TiN-reinforced Al−Mn−Mg−Sc−Zr alloy processed by laser powder bed fusion [J]. Journal of Materials Science & Technology, 2024, 187: 86−100.

[31] DAVID S A, BABU S S, VITEK J M. Welding: Solidification and microstructure [J]. JOM, 2003, 55(6): 14−20.

[32] HOSSEINI S A, ABDOLLAH-ZADEH A, NAFFAKH-MOOSAVY H, MEHRI A. Elimination of hot cracking in the electron beam welding of AA2024-T351 by controlling the welding speed and heat input [J]. Journal of Manufacturing Processes, 2019, 46: 147−158.

[33] ZHAO H, DEBROY T. Weld metal composition change

during conduction mode laser welding of aluminum alloy 5182 [J]. Metallurgical and Materials Transactions B, 2001, 32(1): 163−172.

[34] HU Y N, WU S C, CHEN L. Review on failure behaviors of fusion welded high-strength Al alloys due to fine equiaxed zone [J]. Engineering Fracture Mechanics, 2019, 208: 45−71.

[35] LACHOWICZ M, DUDZIŃSKI W, PODREZ-RADZISZEWSKA M. TEM observation of the heat-affected zone in electron beam welded superalloy Inconel 713C [J]. Materials Characterization, 2008, 59(5): 560−566.

[36] AYAD A, ALLAIN-BONASSO N, ROUAG N, WAGNER F. Grain orientation spread values in IF steels after plastic deformation and recrystallization [J]. Materials Science Forum, 2012, 702/703: 269−272.

[37] FEI Zhen-yu, PAN Zeng-xi, CUIURI D, LI Hui-jun, WU Bin-tao, DING Dong-hong, SU Li-hong, GAZDER A A. Investigation into the viability of K-TIG for joining armour grade quenched and tempered steel [J]. Journal of Manufacturing Processes, 2018, 32: 482−493.

[38] WAN Zhan-dong, WANG Qiang, ZHAO Yue, ZHAO Tian-yi, SHAN Ji-guo, MENG Dan-yang, SONG Jian-ling, WU Ai-ping, WANG Guo-qing. Improvement in tensile properties of 2219-T8 aluminum alloy TIG welding joint by PMZ local properties and stress distribution [J]. Materials Science and Engineering A, 2022, 839: 142863.

[39] CHEN Guo-qing, LIU Jun-peng, SHU Xi, GU Hua, ZHANG Bing-gang, FENG Ji-cai. Beam scanning effect on properties optimization of thick-plate 2A12 aluminum alloy electron-beam welding joints [J]. Materials Science and Engineering A, 2019, 744: 583−592.

[40] WU Ming-yu, XIN Ren-long, WANG Ying, ZHOU Yang, WANG Ke, LIU Qing. Microstructure, texture and mechanical properties of commercial high-purity thick titanium plates jointed by electron beam: Welding [J]. Materials Science and Engineering A, 2016, 677: 50−57.

[41] ZHANG Xin-yi, YANG Wu-xiong, XIAO Rong-shi. Microstructure and mechanical properties of laser beam welded Al−Li alloy 2060 with Al−Mg filler wire [J]. Materials & Design, 2015, 88: 446−450.

[42] FARAJI A H, MORADI M, GOODARZI M, COLUCCI P, MALETTA C. An investigation on capability of hybrid Nd:YAG laser-TIG welding technology for AA2198 Al−Li alloy [J]. Optics and Lasers in Engineering, 2017, 96: 1−6.

[43] DING Ji-kun, WANG Dong-po, WANG Ying, DU Hui. Effect of post weld heat treatment on properties of variable polarity TIG welded AA2219 aluminium alloy joints [J]. Transactions of Nonferrous Metals Society of China, 2014, 24(5): 1307−1316.

[44] ZHU Xin-wen, DENG Ying, LAI Yi, GUO Yi-fan, YANG Zi-ang, FU Le, XU Guo-fu, HUANG Ji-wu. Effects of $Al_3(Sc_{1-x}Zr_x)$ nano-particles on microstructure and mechanical properties of friction-stir-welded Al−Mg−Mn alloys [J]. Transactions of Nonferrous Metals Society of China, 2023, 33(1): 25−35.

[45] SAHUL M, SAHUL M, ORŁOWSKA M, JURČI P, DOMÁNKOVÁ, M, DRIENOVSKÝ, M. Effect of heat input on the microstructure and mechanical properties of electron beam-welded AW2099 aluminium-lithium alloy [J]. Journal of Materials Engineering and Performance, 2024, 33(2): 776−796.

[46] GOLOVIN Y I. Nanoindentation and mechanical properties of materials at submicro- and nanoscale levels: recent results and achievements [J]. Physics of the Solid State, 2021, 63(1): 1−41.

[47] OLIVER W C, PHARR G M. An improved technique for determining hardness and elastic-modulus using load and displacement sensing indentation experiments [J]. Journal of Materials Research, 1992, 7(6): 1564−1583.

[48] CHEN Guo-qing, LIU Jun-peng, DONG Zhi-bo, SHU Xi, ZHANG Bing-gang. Underlying reasons of poor mechanical performance of thick plate aluminum−copper alloy vacuum electron beam welded joints [J]. Vacuum, 2020, 182: 109667.

[49] ZHANG Deng-kui, WU Ai-ping, ZHAO Yue, SHAN Ji-guo, WAN Zhan-dong, WANG Guo-qing, SONG Jian-ling, ZHANG Zhong-ping, LIU Xian-li. Microstructural evolution and its effect on mechanical properties in different regions of 2219-C10S aluminum alloy TIG-welded joint [J]. Transactions of Nonferrous Metals Society of China, 2020, 30(10): 2625−2638.

[50] WANG Da-wei, LIU Zhi-guo, LIU Wen-rui. Experimental study of the electron beam application for evaporation of cobalt, tin and copper [J]. Vacuum, 2023, 209: 111757.

[51] NIU Shao-qiang, YOU Qi-fan, YOU Xiao-gang, SHI Shuang, WANG Yi-nong, TAN Yi. Mechanism of impurities reduction and evaporation of alloying elements for a multi-elements Ni-based superalloy during electron beam remelting [J]. Vacuum, 2018, 156: 345−350.

[52] ZHAN Xiao-hong, CHEN Ji-cheng, LIU Jun-jie, WEI Yan-hong, ZHOU Jun-jie, MENG Yao. Microstructure and magnesium burning loss behavior of AA6061 electron beam welding joints [J]. Materials & Design, 2016, 99: 449−458.

[53] TIAN Jin-tao, CHEN Shuang-jian, LIU Cheng-peng, LEI Guan-hong, YAN Shuai, YE Xiang-xi. Investigation on solidification crack susceptibility for weld metals of GH3539 alloy with Trans-Varestraint test [J]. Materials Today Communications, 2024, 41: 110898.

[54] PUJONO, ILMAN M N, KUSMONO, MUSLIH M R, PRIYANTO T H, APRIANSYAH R, ISNAINI A. Diminishing residual stress and distortion by in-situ rolling tensioning to increase fatigue performance of friction stir welded AA2024-T3 joints [J]. International Journal of Fatigue, 2025, 190: 108659.

[55] NOELL P J, CARROLL J D, BOYCE B L. The mechanisms of ductile rupture [J]. Acta Materialia, 2018, 161: 83−98.

[56] WU Lai-jun, HAN Xiao-hui, MA Guo-long, YANG Biao, BIAN Hong, SONG Xiao-guo, TAN Cai-wang. Effects of welding layer arrangement on microstructure and mechanical properties of gas metal arc welded 5083/6005A aluminium alloy butt joints [J]. Transactions of Nonferrous Metals Society of China, 2023, 33(6): 1665−1676.

电子束焊接 5B70 铝合金接头的显微组织演变及力学性能

张宇鹏[1]，金 国[1]，董丽虹[2]，崔秀芳[1]，高 冲[3]，谢向宇[1]，底月兰[2]，
郭伟玲[2]，宋牙牙[2]，石文静[4]，曾如川[5]，黄 宁[5]

1. 哈尔滨工程大学 材料科学与化学工程学院，超轻材料与表面技术教育部重点实验室，哈尔滨 150001;
2. 陆军装甲兵学院 再制造技术国家重点实验室，北京 100072;
3. 辽宁工业大学 机械工程与自动化学院，锦州 121001;
4. 北京空间飞行器总体设计部，北京 100094;
5. 北京卫星制造厂有限公司，北京 100089

摘 要：研究了航空航天 5B70 铝合金真空电子束焊接接头的显微组织演变和力学性能。采用 X 射线衍射、扫描电子显微镜和电子背散射衍射对相组成、显微组织演变、晶粒尺寸、晶界密度和织构变化进行了定量分析。熔合区(FZ)由等轴胞状晶组成，在熔合区和热影响区(HAZ)之间的过渡区(TZ)形成约 20 μm 厚的细晶层。热影响区与基材(BM)非常相似，保留了原始的轧制组织。力学性能测试表明，TZ 中的细晶层具有最高的纳米硬度，而 FZ 的显微硬度最低。焊接接头试样的屈服强度、极限抗拉强度和断裂伸长率均低于 BM，其主要受晶粒尺寸和析出相分布的影响。

关键词：5B70 铝合金；真空电子束焊接；晶体结构；纳米硬度；拉伸性能

(Edited by Xiang-qun LI)